Identification of a double decay length (λ^t_q) heat flux deposition shape with embedded thermal measurement and neural network

Y. Anquetin, J. Gaspar, Y. Corre, Jl Gardarein, J. Gerardin, P. Malard, F. Rigollet, Q. Tichit, E. Tsitrone

Nuclear Materials and Energy 41 (2024) 101788

Contents lists available at ScienceDirect

Nuclear Materials and Energy

journal homepage: www.elsevier.com/locate/nme

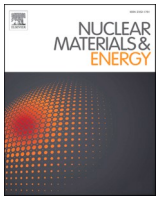

Identification of a double decay length (λ_q^t) heat flux deposition shape with embedded thermal measurement and neural network

Y. Anquetin [a], J. Gaspar [a], Y. Corre [b], JL. Gardarein [a], J. Gerardin [b], P. Malard [b], F. Rigollet [a], Q. Tichit [b], E. Tsitrone [b], the WEST team[1], the EUROfusion Tokamak Exploitation team[2]

[a] Aix Marseille Univ, CNRS, IUSTI, Marseille, France
[b] CEA, Institute for Research on Fusion by Magnetic confinement, 13108 St-Paul-Lez-Durance, France

ARTICLE INFO

Keywords:
Tokamak
WEST
Divertor
Heat flux
Decay length
Neural network

ABSTRACT

The estimation of the heat flux density distribution profiles in tokamak devices is a very important research topic for edge plasma physics purposes and also to ensure the safety of the machine. In the radial direction, the heat flux exhibits an exponential decay that could be captured by thermal sensors distributed in the plasma facing components. Radially distributed thermal sensors based on Fiber Bragg grating technology have been embedded in the WEST lower divertor to study the heat flux deposition profiles during plasma operation. The comparison between embedded measurements and a 3D finite element model shows a small decay length (5 – 10 mm) on top of a wider heat flux with a decay length around 30 to 50 mm. A tool using neural network has been developed in order to predict the values of the different parameters describing the deposited heat flux from embedded temperature measurements in steady state. A large span of deposited heat fluxes with maximum heat flux ranging from 1 to 9 MW/m^2 and decay length from 5 to 50 mm were characterized using this tool over a database of more than 250 experimental L-mode pulses performed in WEST in attached divertor configuration. The comparison of the predicted heat flux parameters values with macroscopic plasma parameters have revealed the appearance of the narrow component with the increase of the divertor power load (P_{div}) with a threshold dependant of the plasma current (I_P).

Introduction

One of the main objectives of WEST is the testing of the actively cooled tungsten Monoblock (MB) technology foreseen for ITER divertor in a tokamak environment. To do so, WEST lower divertor technology and design are following exactly the specifications of ITER divertor vertical targets. The plasma facing units (PFU) of the divertor are designed to sustain heat flux going up to 10 MW/m^2 in steady state and up to 20 MW /m^2 during slow transient. To evaluate the heat exhaust capability and the temperature behaviour of these components, different diagnostics are monitoring the divertor components. Langmuir probes are monitoring the particles flux and edge plasma temperature, infrared thermography is checking the surface temperature of the divertor and embedded thermal diagnostics are used to obtain temperature inside the MB, thus without any parasitic surface-related effects. This work focus on the exploitation of thermal embedded measurements performed with Fibre Bragg Gratings (FBG) technology [1,2]. In WEST, the FBGs are located 5 mm below the divertor surface on the trailing edge of the component [3]. The goal is to compute the heat flux distribution on the top of the PFU from these thermal measurements. To do so, a tool using neural network has been developed and allows to predict the deposited heat flux shape and intensity from multiple embedded thermal measurements. In the first part of this paper, the WEST lower divertor as well as the sensors used in this work are presented. The second part of this article presents the identification and validation of a double decay length heat flux deposition shape from the measurements made in WEST. A third part will present the development of a tool using neural network to predict the surface heat flux from embedded measurement. Finally, the results of our prediction on a database of more than 250 experimental L-mode pulses in attached divertor configuration will be presented and compared with macroscopic plasma parameters.

[1] http://west.cea.fr/WESTteam.
[2] See the author list of "Overview of the EUROfusion Tokamak Exploitation Programme in Support of ITER and DEMO" by E. Joffrin Nuclear Fusion 2024.

https://doi.org/10.1016/j.nme.2024.101788
Received 5 July 2024; Received in revised form 1 October 2024; Accepted 22 October 2024
Available online 24 October 2024

WEST lower divertor and embedded thermal measurement

From the C7 experimental campaign performed in 2023, WEST lower divertor was fully equipped with ITER-grade PFU [4]. It consists of a full tungsten actively cooled divertor divided into 12 toroidal sectors (30° toroidal extension), each made of 38 PFUs. Each PFU is made up of 35 tungsten MBs arranged in the poloidal direction along a copper pipe for cooling. The Fig. 1 presents in **A.** a view of the full divertor with a close up on one 30° sector. Figure **B.** shows a close up on one PFU instrumented with FBG embedded 5 mm below the surface of the component (here on the outer side of the divertor). This diagnostic allows to measure the temperature up to 1000 °C on 14 locations along the PFU, one measurement point every 12.5 mm, using an acquisition frequency of 10 Hz. The FBG sensors are positioned in the middle of the 12 mm width MB, 5 mm below the top surface of the MB to avoid temperature exceeding 1000 °C (technical limitation), on the trailing edge. In the following studies, only 11 measurements are exploited due to the magnetic shadowing of the baffle on the divertor PFUs presented in Fig. 2 **B.** The monitoring and comprehension of these heat fluxes in the scrape-off layer (SOL) is mandatory to ensure the safety of the divertor as well as the machine and evaluate heat exhaust capabilities of the PFUs tested in WEST.

Fig. 2 presents the FBG measurements during one typical 500kA, dX = 69.4 mm, 4 MW injected LH power pulse in WEST. Fig. 2 **A.** presents, for each grating, the temporal evolution of the heating of each MB ($\Delta T = T_{FBG}\text{-}T_{water}$, where T_{FBG} is the FBG measurement and with T_{water} = 70 °C as operated in most of the WEST experiments). This allows us to evaluate the stability of the pulse and checking the most exposed MB. The thermal response of the FBG sensor is longer than the time to reach the thermal equilibrium of the MB. The time to reach 90 % of the stabilized temperature is typically 5 s with the ITER PFU. With the FBG system, the stabilized temperature is obtained after 10 s for the probe presented in Fig. 2 **A.**. Fig. 2 **B.** which represents the profile of heating is plotted using the measurement of each grating averaged over a time period at thermal equilibrium (here between $t_{beginning} = 35s$ and $t_{end} = 40s$). Heating profiles can be used to predict deposited heat fluxes in steady state, which is the focus of this paper. Validation of a method for transient problem for ITER-grade PFU is presented in [5].

Deposited heat flux shape: Observation of double decay length in thermal measurement

Due to the limited number of measurements, an a priori is needed to describe the evolution of power in the SOL. The convolution of an exponential with a Gaussian as expressed in *Eich et al.* [6] is considered a reference in the fusion community to describe the heat flux distribution in the radial/poloidal direction. This heat flux deposition shape was characterised for ELM-free, H-mode pulses but still is usable for L-mode pulses as shown in the work of Scarabasio *et al.* [7]. During WEST first phase of operation, with inertial tungsten coated graphite components in the divertor and assuming this distribution, heat fluxes presenting decay length ranging from 10 mm to 60 mm were observed [8]. With the second phase of operation in WEST, the whole divertor has been changed to ITER-grade actively cooled bulk tungsten castellated plasma facing unit [9,10]. The plasma control system was also improved allowing better stability for the position of the strike line enabling to stabilize the temperature of the MB during the plasma experiment. With this evolution and progress with the operational domain, a narrow heat flux component is needed to match some of the measurements with numerical modelling. The sum of two different heat flux distribution profiles, each following *Eich et al.* distribution but with two different decay lengths is considered as the total deposited heat flux, also seen in Asdex-Upgrade [11], or JET [12,13]. The Equations (1) & (2) presents *Eich et al.* classical deposition shape and the two decay length shapes, respectively. With the maximum heat flux for a pure exponential: ϕ_{m_0}, in the rest of this paper the exact maximum heat flux ϕ_m will be used, the background heat flux: ϕ_{BG}, the strike line (separatrix) position: x_0 and the spreading factor on the target in the private region: S^t, the heat flux decay length on the target: λ_q^t larger than the decay length on the mid-plane by the factor of magnetic expansion.

$$\phi(x) = \frac{\phi_{m_0}}{2} exp\left[\left(\frac{S^t}{2\lambda_q^t}\right)^2 - \frac{x-x_0}{\lambda_q^t}\right] * erfc\left(\frac{S^t}{2\lambda_q^t} - \frac{x-x_0}{S^t}\right) + \phi_{BG} \quad (1)$$

Equation (1): Classical 1 decay length Eich et al. deposition shape

$$\phi(x) = \frac{\phi_{m_{narrow0}}}{2} exp\left[\left(\frac{S^t}{2\lambda_{q_{narrow}}^t}\right)^2 - \frac{x-x_0}{\lambda_{q_{narrow}}^t}\right] * erfc\left(\frac{S^t}{2\lambda_{q_{narrow}}^t} - \frac{x-x_0}{S^t}\right) + \frac{\phi_{m_{far0}}}{2} exp\left[\left(\frac{S^t}{2\lambda_{q_{far}}^t}\right)^2 - \frac{x-x_0}{\lambda_{q_{far}}^t}\right] * erfc\left(\frac{S^t}{2\lambda_{q_{far}}^t} - \frac{x-x_0}{S^t}\right) + \phi_{BG} \quad (2)$$

Equation (2): Double decay length Eich et al. Deposition shape with a narrow contribution and a far contribution

Fig. 3 presents in **A.** measured (black circles) and computed heating for the pulse shown in Fig. 2 considering the 1 and 2 decay lengths heat flux shapes. In this pulse, the peak heat flux is found on MB25. The background heat flux is computed in the private area (between MB20 and MB22). For this pulse it is evaluated to $\phi_{BG} = 51 kW/m^2$. Comparing the green triangles (1 decay length) with the black circles (experimental points), the 1 decay length model gives higher temperature on MB26, and lower temperature for MB 28 to 30. Meanwhile the purple crosses are following almost perfectly the measurement. These temperatures are

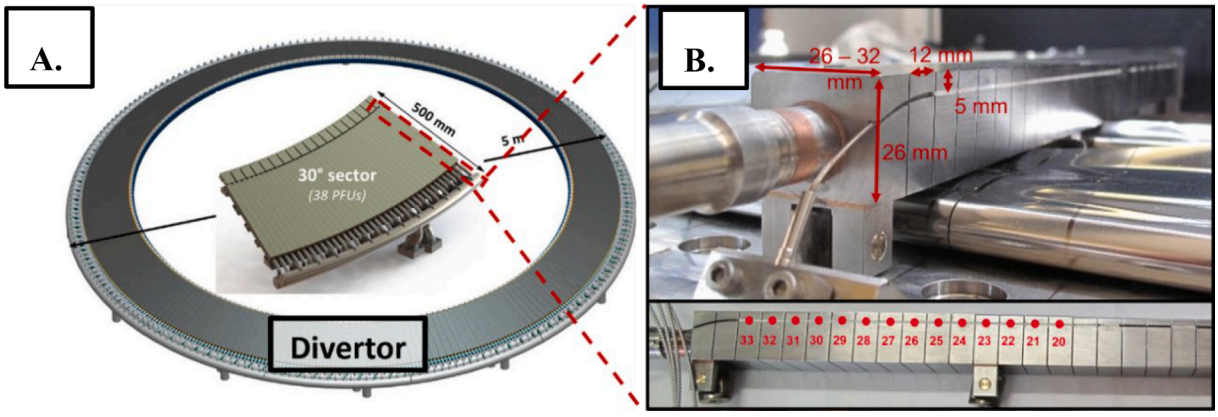

Fig. 1. A. view of WEST complete lower divertor and sector, **B.** WEST ITER-grade PFU with embedded FBG (outer probe).

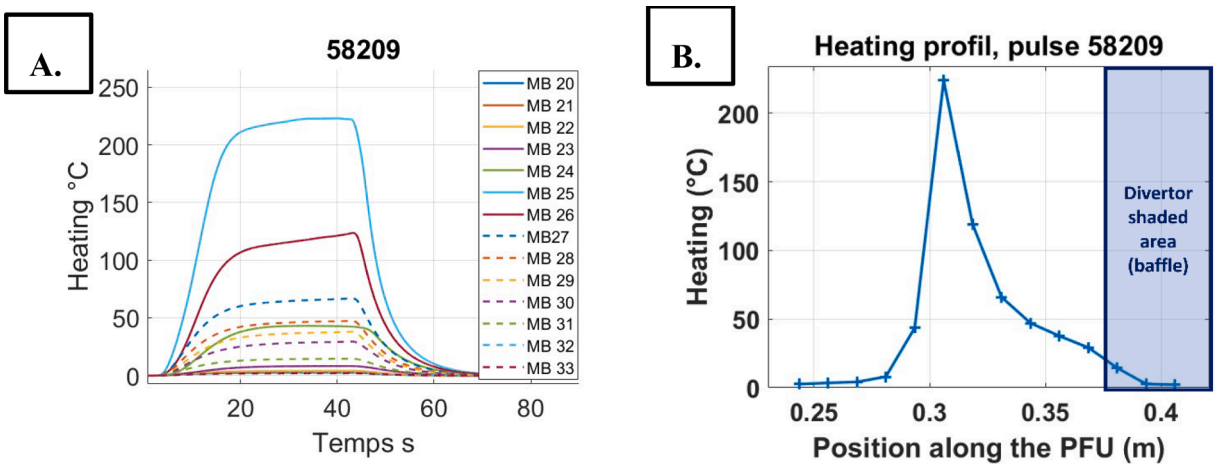

Fig. 2. Measurement in WEST with embedded FBG on the **outboard** part of the divertor, **A. Measured** heating during pulse 58209, **B.** Heating profile during steady state (between 20 and 40 s).

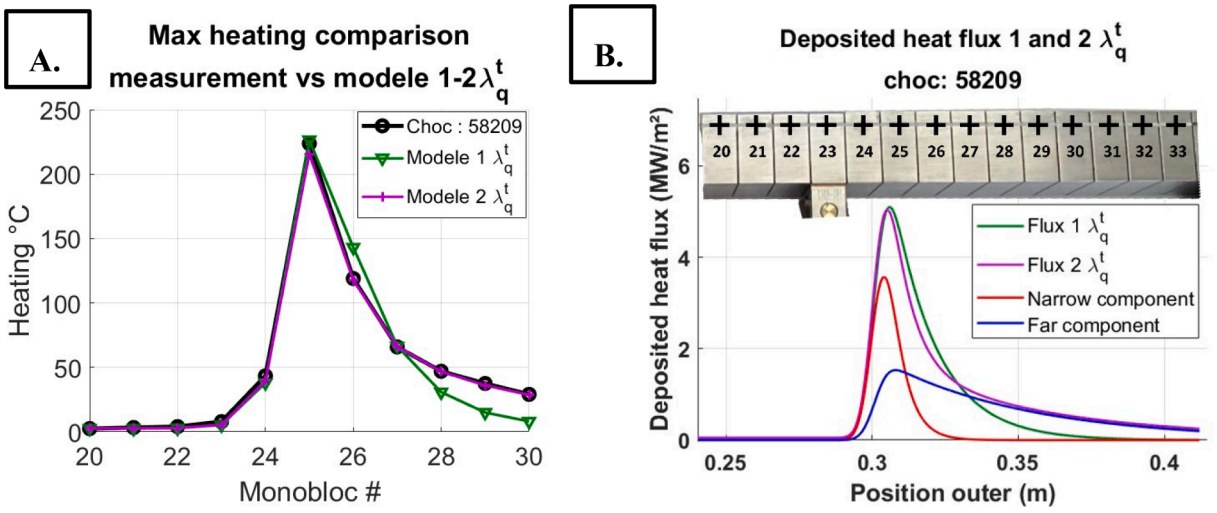

Fig. 3. Comparison of 1 and 2 decay length for the experimental pulse 58209, **A.** Heating profiles measured (black), fit 1 λ_q^t model (green), fit 2 λ_q^t model (magenta), B. Deposited heat fluxes1 λ_q^t model (green), 2 λ_q^t model (magenta), narrow component for 2 λ_q^t model (red), far component for 2 λ_q^t model (blue), location of the FBG gratings for temperature measurement (black cross marker) on the PFU.

Table 1
Heat flux distribution parameter, for model 1 λ_q^t and pulse #58209.

$\phi_{m_{narrow}}$	$\lambda^t_{q_{narrow}}$	x_0	ϕ_{BG}	S
5.1E6 W/m^2	15 mm	301 mm	51 kW/m^2	2 mm

obtained using the double decay length heat flux shape model with the values for the narrow and far component of the heat flux presented on Fig. 3 **B.** The heat fluxes distribution parameters values are specified in Table 1 for 1 λ_q^t model and Table 2 for 2 λ_q^t model. Despite the modification of the global shape, the total maximum heat flux remains unchanged. In Fig. 3 **B.** the closest fit is obtained with a total maximum heat flux of 5.1 MW/m^2 for both deposition shape. The narrow contribution, representing 70 % of the peak heat flux, shows much smaller decay length compared to the averages values observed in WEST during its first phase of operation (5 mm vs ~ 20 mm) [8]. The far contribution allows to fit the measurement for MB 28 to 30 with a smaller influence on the peak heat flux but a very large decay length (50 mm). However, due to the small decay length for the narrow contribution, less power is channelled in the narrow contribution than the far one. In this example, the integral of the heat flux along the radial distance represents 46 kW/m in the narrow contribution and 80 kW/m in the far contribution.

Table 2
Heat flux distribution parameter, for model 2 λ_q^t and pulse #58209.

$\phi_{m_{narrow}}$	$\phi_{m_{far}}$	$\lambda^t_{q_{narrow}}$	$\lambda^t_{q_{far}}$	x_0	ϕ_{BG}	S
3,57E6 W/m^2	1,53E6 W/m^2	5 mm	50 mm	301 mm	51 kW/m^2	2 mm

It has been validated those measurements presenting only one decay length cannot be obtained using a two exponential deposition shape independently of the position and vice versa.

Development of a neural network based prediction tool

The following part presents the development of a neural network prediction tool designed to predict the deposited heat flux parameter (ϕ_m, λ_q^t, x_0…) values based on FBG temperature measurements. This kind of problem is called regression and is best solved using multilayer perceptron (MLP) neural network. A MLP is a deep learning neural

network [14] which means that the output is linked to the input by a succession of layers, each made of a specific number of nodes. The number of layer define the depth (from deep learning) of the neural network and the number of nodes define it's width. Different methodologies (decomposition in multiple neural networks), depth and width were tested to obtain the best predictions of the parameters using TensorFlow, Keras library [15].

Two different MLP are needed to predict the two different heat flux shapes with a different number of parameters. Numerical temperatures are computed using a 3D model of the PFU developed with finite element method using Cast3m software [16,5]. A wide range of plausible deposited heat fluxes are then used in order to train the neural networks. Table 3 presents the number of referential simulated data used to train our neural networks as well as the range of values for each parameter (peak heat flux, heat flux decay length, position of the peak and background flux). Table 3 shows that some heat fluxes distribution used to train our neural network present only one decay length ($\phi_m = 0$). This choice is motivated to include most deposition shape possibles. Due to the large number of possibilities, considering a double exponential shaped deposited heat flux, more referential pulses were considered. The exact values for each case were defined using Halton sequence. A single value for the spreading factor in the private flux region is considered ($S = 2$), based on the observations made using infrared diagnostics in WEST [17] to limit the number of training data to compute. Despite this simplification, the temperatures from more than 350,000 different heat fluxes distributions and intensities were computed in steady state.

The development of a neural network can be split into 3 steps repeated until a satisfactory result is reached. First, the conception of the neural network: in this step, the user defines a number of parameters, called hyperparameters, that will define the architecture of the network. The number of hidden layers or nodes for each layer are good examples of hyperparameters. Once the architecture is defined, come the tuning of the network. Based on the training data, an algorithm will find the good weight for each node so that the desired output appears from multiplication between node and input data. This part uses automatic algorithms and can be quite long depending on the complexity of the model as well as the number of training data. Once the model is trained, it is necessary to ensure that it is able to generalize the resolution of the problem with new data unused during the training part. In this case, the total number of referential pulses were divided in three categories: the training set representing 70 % of the pulses, chosen randomly, 15 % for the validation during training and 15 % for the test after training [14]. During the training phase as well as for the testing after training, different quantities are tracked to evaluate the performance of the model. The "mean absolute error" (mae) or "mean squared error" (mse) are good indicators to track the discrepancies between the result of the model and the real data.

Finally, two different models using different architecture were defined. The first one is using a single neural network predicting the 4 parameters characterizing the heat flux parameters for the 1 decay length model, based on 11 temperatures measurements. The second one, for the 2 decay length model, is based on two different neural networks. With a first neural network, the parameters ϕ_{BG} and x_0 are predicted using the measurements from gratings MB20 to MB22 (located in the private flux region, thus exposed to plasma radiation and neutral particles only), the measurements and positions of the 2 gratings around the maximum heating. Then, from a second neural network, $\boldsymbol{\phi}_{\boldsymbol{m}_{narrow}}$, $\boldsymbol{\lambda}^{\boldsymbol{t}}_{\boldsymbol{q}_{narrow}}$, $\boldsymbol{\phi}_{\boldsymbol{mfar}}$ and $\boldsymbol{\lambda}^{\boldsymbol{t}}_{\boldsymbol{q}_{far}}$ are predicted using the 11 measured temperatures plus the previously predicted $\boldsymbol{x}_0$ and $\boldsymbol{\phi}_{\boldsymbol{BG}}$. Each neural network is made of dense layer, fully connected. The final architectures are summarized in Table 4.

Table 3
Numerical training data for 1 and 2 λ^t_q heat fluxes prediction neural networks.

Model		Ref. pulses #	Parameters values span				
			ϕ_m MW/m^2	λ^t_q mm	x_0 mm	ϕ_{BG} kW/m^2	S mm
$1\lambda^t_q$		~ 56,000	0.1 – 10	5 – 50	275 – 362	0 – 125	2
$2\lambda^t_q$	Narrow	~ 300,000	0 – 6	2 – 15	275 –	0 – 250	2
	Far		0 – 6	15 – 50	362		

These tools are applied on a database of 275 experimental L-mode pulses in WEST in attached regime. Table 5 present the span of some plasma parameters for these pulses, P_{div} being the divertor power load calculated as the difference between heating power (ohmic and LH mainly) and the power radiated by the plasma. dX is the X point height obtained using WEST magnetic reconstruction.

Fig. 4 **A.** and **B.** present the best fits, for two different experimental pulses in WEST, between the measured and computed temperatures assuming the heat flux predicted by our neural networks. Fig. 4 **A.** shows a fit for one pulse evaluated with 1 decay length and Fig. 4 **B.** for a pulse with 2 decay lengths. The values for each parameter are given in the figure caption and the plasma properties in the legend. A good agreement between computed and measured temperatures is observed when using the appropriate model.

For each case the mean discrepancies per grating normalized using the maximum temperature is computed in order to evaluate the performances of these tools. The results of this criterion are presented in Fig. 5 and shows a mean error ~ 0.5 % of the maximum temperature for each grating when using the appropriate model. Fig. 5 shows the stability of the predictions for repetitive pulses (pulses #100 to #220) as mentioned in following section 5.1. The pulses ranging from #100 to #220 are realised using the same plasma scenario. Similar heating profile are measured for these pulses leading to stable predictions and error. This criterion is used to automatically define if the deposited heat flux is closer to the 1 or 2 exponential shapes. This demand for each pulse to compute the results of the 2 models demanding ~ 1 min each. This calculation is mandatory to ensure the results due to the inherent black box system of neural networks. These results has been compared with those of an inverse method using conjugate gradient (MGC), presented and validated in [5] for the pulse #57824. Comparison of estimated heat flux (MGC) and the predicted heat flux (neural network) shows good agreement and are presented in Table 6.

Comparison with infrared diagnostics were made using data from the very high resolution camera in WEST for a specific pulse and shows good agreement for the heat flux deposition shape narrow component. These observations should be the object of future publication.

Results of AI based predictions

The deposited heat flux shape and intensity can now be predicted automatically for every pulse in WEST. It is now possible to characterize the heat flux during experimental campaigns between two pulses so in a time interval of 10 to 15 min in WEST.

High fluence campaign: Robustness of the predictions

During the 2023 experimental campaign, a long "high fluence" dedicated campaign (HFC) was done [18]. During this campaign, more than 100 repetitive pulses (injected LH power: 3.8 MW, plasma current: 399 kA, plasma density: $3.7*10^{17}$ m^{-3}, dX: 70 mm) were executed in order to maximize the particle fluence on the divertor components. This campaign is a good opportunity to test the robustness of our neural networks, as the heat flux should be the same pulse to pulse. The following Fig. 6 **A.** and **B.** present the result of the predictions during the HFC. Consistent parameters prediction is observed once the final tuning

Table 4
Final architectures of the three neural networks.

	Inputs	Outputs	Layer #	Node # per layer L_i	Activation function
$1\lambda_q^t$	11 temperatures	$\phi_m, \phi_{BG}, \lambda_q^t, x_0$	9	$L_{input} = 11$; $L_1 = 1024$; $L_{2\to7} = 512$; $L_8 = 256$; $L_9 = 128$; $L_{output} = 4$	relu
$2\lambda_q^t$	6 temperatures, 2 positions	ϕ_{BG}, x_0	4	$L_{input} = 8$; $L_1 = 64$; $L_2 = 32$; $L_{3\to4} = 16$; $L_{output} = 2$	relu
	11 temperatures, ϕ_{BG}, x_0	$\phi_{m_{narrow}}, \phi_{m_{far}}, \lambda^t_{q_{narrow}}, \lambda^t_{q_{far}}$	4	L_{input} : 13; L_1 : 256; L_2 : 128; $L_{3\to4}$: 32; L_{output} : 4	relu

Table 5
Plasma parameters span for the processed experimental pulses in WEST.

	LH heating power (MW)	P_{div}(MW)	Plasma current I_p(kA)	Plasma core density (10^{19} m^{-3})	dX (mm)
Minimum	6.64e-05	0.18	299.5	2.49	58
Maximum	5.784	3.52	499.5	4.46	81

of the scenario is made. The heat flux presented in Fig. 6 **A.** is splitted between 2/3 in the narrow component and 1/3 in the far component with an averaged maximum heat flux $\phi_{m_{tot}} \cong 5MW/m^2$. A small decrease of the peak heat flux is observed which is consistent with the small increase of the radiated power also observed during the HFC (from 50 % at the beginning to 55 % radiated power fraction at the end of the HFC as reported in [19]). Fig. 6 **B.** presents the predicted values of $\lambda_q^t narrow$ and $\lambda_q^t far$ also constant after the final tuning. An average narrow decay length of 8 mm and a far decay length of 45 mm are observed.

Parameters prediction

Over the whole 2023 campaign, a wide range of plasma pulses were performed (different plasma current, densities, magnetic equilibrium and injected power). The experimental data base is built on pulses featuring steady state heat load long enough to reach the thermal equilibrium of the PFU. The following Fig. 7 **A.** presents for every selected pulse the total predicted heat flux depending on the power on the divertor. Different behaviour are observed between the pulses evaluated with 1 or 2 decay lengths regarding the predicted heat flux. For the same P_{div}, it appears from figure **A.** that the heat fluxes presenting a narrow component displays higher maximum total heat flux compared to single decay length heat fluxes. Fig. 3 in section 3 shows that this difference is not due to the model used for the fit as the same maximum heat flux is obtained for the same pulse with the two different

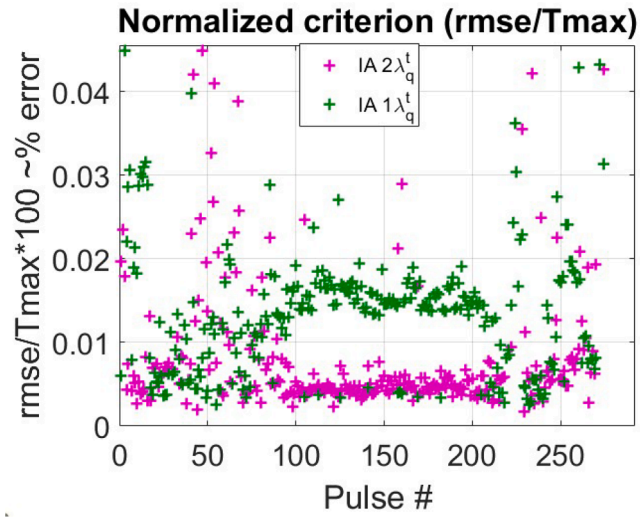

Fig. 5. Normalized criterion for neural networks performances evaluation.

Table 6
Comparison of the heat fluxes estimated using the MGC and predicted with the neural network (1 λ_q^t) for the pulse #57824.

	ϕ_m(MW/m^2)	ϕ_{BG}(kW/m^2)	λ_q^t(mm)	S (mm)	x_0(mm)
Estimations MGC (ϕ_m&ϕ_{BG} moyennés)	1,28	27,3	27,2	2	298,7
Prédictions IA	1,17	51,8	28,4		299,0
Error	**8,6 %**	**89,7 %**	**4,2 %**		**0,1 %**

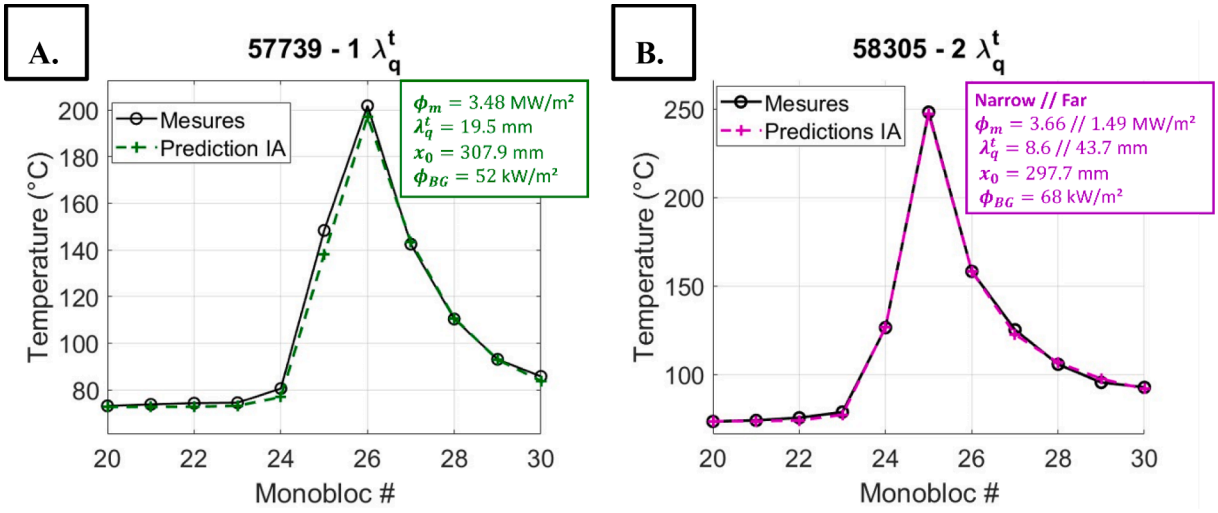

Fig. 4. Fit of experimental measurement with numerical temperature assuming surface heat fluxes predicted using AI, **A.** for 1 λ_q^t, I_p = 499 kA, P_{div} = 1.97 MW, plasma density = 3.97*10^{17} m^{-3}, dX = 75.1 mm, **B.** for 2 λ_q^t, I_p = 399 kA, P_{div} = 1.95 MW, plasma density = 3.76*10^{17} m^{-3}, dX = 70.4 mm.

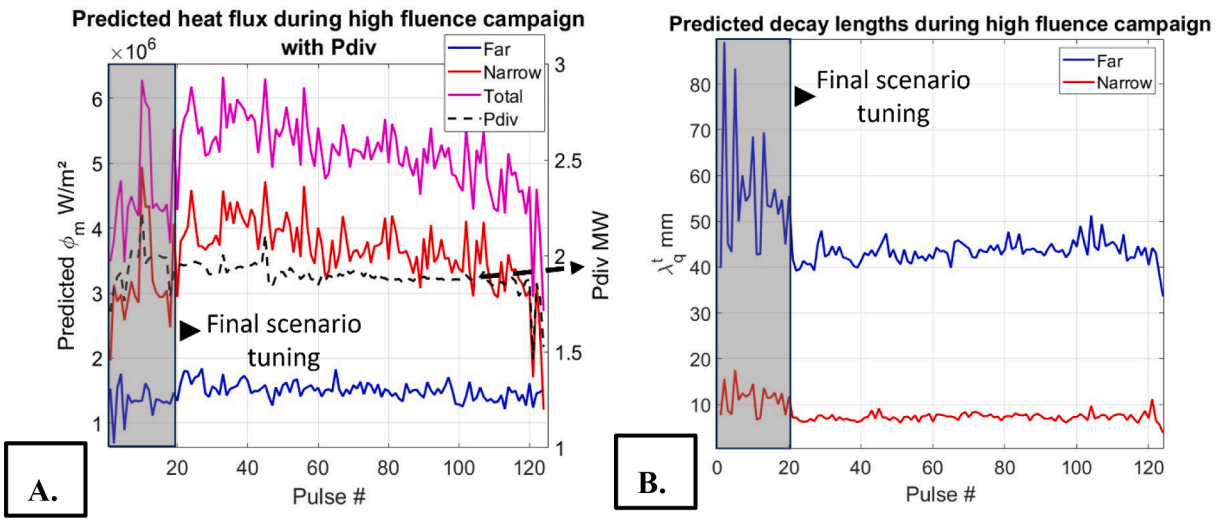

Fig. 6. Predicted heat fluxes parameters for HFC, **A.** maximum heat fluxes, **B.** decay lengths.

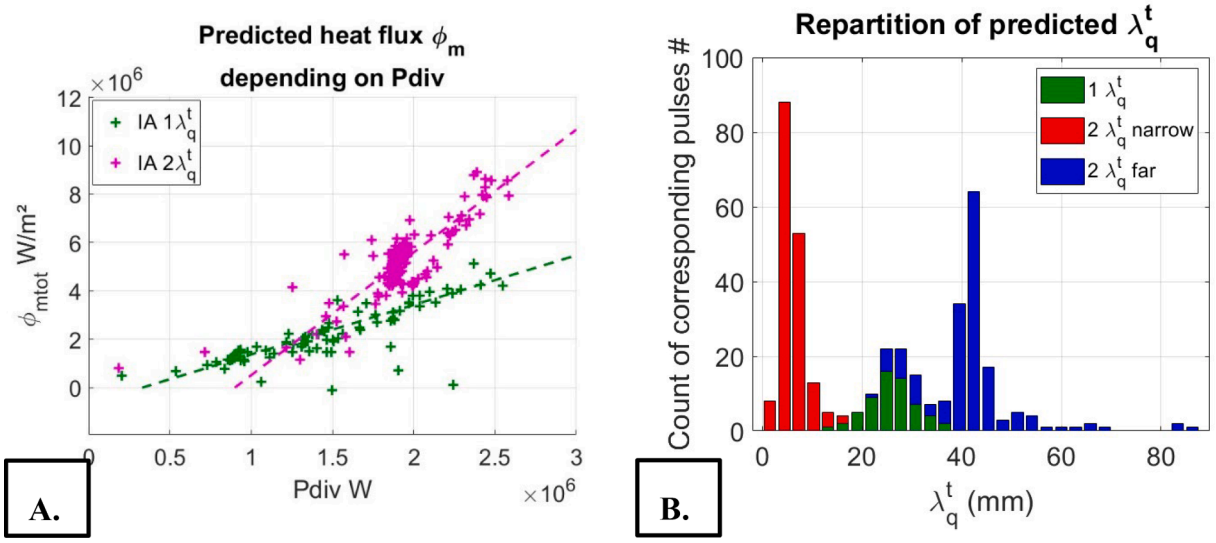

Fig. 7. Range of predicted parameters values, **A.** total maximum heat fluxes depending on the power on the divertor, **B.** stacked histogram of predicted decay lengths.

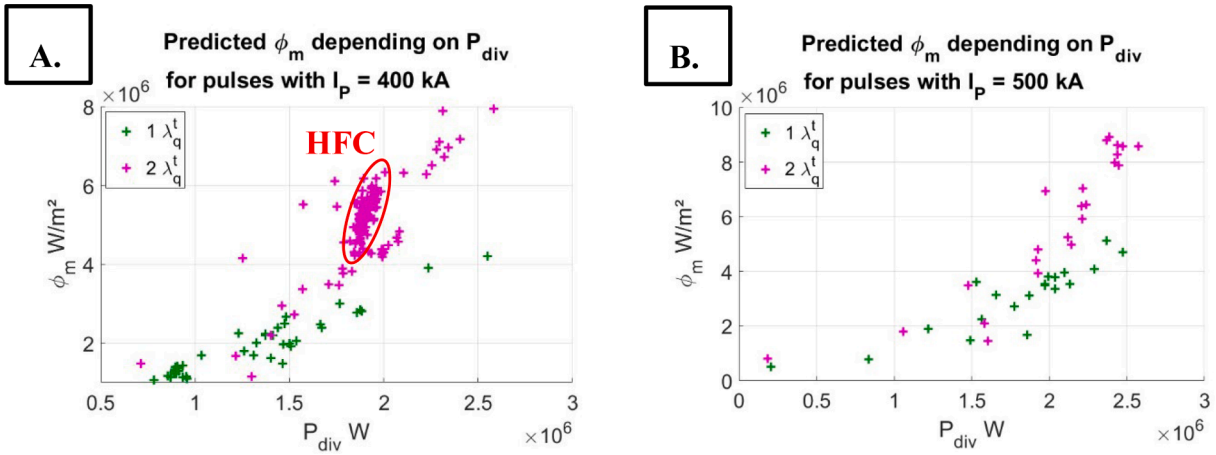

Fig. 8. Results of predicted maximum heat flux depending on P_{div}, **A.** for I_p = 400 kA, **B.** for I_p = 500 kA.

model. The maximum heat flux reported in the C7 data base is 9 MW/m^2 with 2.5 MW power in the divertor, value which is close to the nominal heat load expected in ITER.

Fig. 7 **B.** shows the range of predicted decay lengths in our measurement. 3 different populations are observed with small overlapping mainly between the far population (in blue) and the 1 λ_q^t population (in green). Half the pulses have a far λ_q^t between 25 mm and 31 mm and the other half between 37 and 45 mm. The narrow component (in red) lies mainly between 2 and 20 mm, with a peak between 2 and 10 mm. Such sharp heat fluxes could be harmful to the divertor components causing local over-heating or melting of the PFU and need to be monitored.

Plasma current (I_p) impact on narrow part appearance

The causes of these two different populations are not understood yet. Some evidences point a relation between the appearance of the narrow component and an increase of the power on the divertor with a threshold value of P_{div} depending on the plasma current I_p. Fig. 8 **A.** and **B.** show the maximum heat flux predicted depending on the P_{div} with $I_p = 400$ kA and $I_p = 500$ kA for **A.** and **B.**, respectively. Fig. 8 **A.** shows that above $P_{div} = 1.8$ MW, almost no pulses are evaluated with only one decay length and most of the pulses with 2 decay lengths. The HFC pulses are gathered in the red circle. Whereas there is no clear transition for $I_p = 500$ kA. More analysis and probably dedicated experiment with a scan in I_p and power will be needed in order to confirm these relations. The role of plasma density profiles and neutral particles distribution could also be investigated in the far SOL.

Conclusion

Thermal embedded measurements performed in the WEST lower divertor ITER-grade PFUs have shown a 2 decay lengths shape in the deposited heat flux poloidal profile. A narrow component with a decay length $\lambda_q^t = 5-15mm$ has been identified on top of a wider heat flux with a decay length $\lambda_q^t = 30-50mm$ during the high power pulses ($P_{div} > 1.8$ MW). The development of a neural network based prediction tool trained with numerical temperatures allowed us to characterize heat fluxes going up to almost 9 MW/m^2. The method has been tested on the high fluence campaign first. The results shows constant values for the heat flux decay length (8 mm for the narrow and 45 mm for the far components respectively) and peak heat flux of about 5.5 MW/m^2 in the beginning of the campaign, down to 4.7 MW/m^2 in the end of the campaign which is also consistent with the slow increase of radiated power observed during the HFC. The method has also been applied to the full experimental campaign. Two populations are clearly observed, with one or double heat flux decay lengths. However, the origin of these two different forms of heat flux observed in WEST has not been found yet. A relation between power on the divertor, plasma current and shape seems to appear in our data. Complementary experiments during future experimental campaigns need to be done to prove or discard these observations, such as a scan of plasma current and power.

CRediT authorship contribution statement

Y. Anquetin: Writing – review & editing, Visualization, Validation, Resources, Methodology, Investigation, Data curation. **J. Gaspar:** Writing – review & editing, Visualization, Validation, Supervision, Software, Methodology, Investigation, Formal analysis, Data curation. **Y. Corre:** Writing – review & editing, Visualization, Validation, Resources, Methodology, Investigation, Data curation. **JL. Gardarein:** Writing – review & editing, Supervision. **J. Gerardin:** Writing – review & editing, Visualization, Validation, Supervision, Software, Methodology, Investigation, Formal analysis, Data curation. **P. Malard:** Writing – review & editing, Resources, Data curation. **F. Rigollet:** Writing – review & editing, Methodology, Investigation, Formal analysis. **Q. Tichit:** Writing – review & editing, Validation, Investigation. **E. Tsitrone:** Writing – review & editing, Validation, Project administration.

Declaration of competing interest

The authors declare that they have no known competing financial interests or personal relationships that could have appeared to influence the work reported in this paper.

Acknowledgments

This work has been carried out within the framework of the EUROfusion Consortium, funded by the European Union via the Euratom Research and Training Programme (Grant Agreement No 101052200 — EUROfusion). Views and opinions expressed are however those of the author(s) only and do not necessarily reflect those of the European Union or the European Commission. Neither the European Union nor the European Commission can be held responsible for them.

Data availability

The authors do not have permission to share data.

References

[1] Y. Corre *et al.*, *Rev. Sci. Instrum.*, vol. 89, n° 6, p. 063508, juin 2018, doi: 10.1063/1.5024514.
[2] G. Laffont, R. Cotillard, N. Roussel, R. Desmarchelier, et S. Rougeault, *Sensors*, vol. 18, n° 6, p. 1791, juin 2018, doi: 10.3390/s18061791.
[3] N. Chanet *et al.*, *Fusion Eng. Des.*, vol. 166, p. 112376, mai 2021, doi: 10.1016/j.fusengdes.2021.112376.
[4] J. Bucalossi, et al., Nucl Fusion (2022), https://doi.org/10.1088/1741-4326/ac2525.
[5] Y. Anquetin *et al.*, *Fusion Eng. Des.*, vol. 190, p. 113480, mai 2023, doi: 10.1016/j.fusengdes.2023.113480.
[6] T. Eich *et al.*, *Phys. Rev. Lett.*, vol. 107, n° 21, p. 215001, nov. 2011, doi: 10.1103/PhysRevLett.107.215001.
[7] A. Scarabosio, T. Eich, A. Herrmann, et B. Sieglin, *J. Nucl. Mater.*, vol. 438, p. S426-S430, juill. 2013, doi: 10.1016/j.jnucmat.2013.01.086.
[8] J. Gaspar *et al.*, *Nucl. Fusion*, vol. 61, n° 9, p. 096027, sept. 2021, doi: 10.1088/1741-4326/ac1803.
[9] M. Missirlian *et al.*, *Fusion Eng. Des.*, vol. 89, n° 7-8, p. 1048-1053, oct. 2014, doi: 10.1016/j.fusengdes.2014.01.050.
[10] J. Bucalossi *et al.*, *Fusion Eng. Des.*, vol. 89, n° 7-8, p. 907-912, oct. 2014, doi: 10.1016/j.fusengdes.2014.01.062.
[11] T. Lunt *et al.*, *Nucl. Mater. Energy*, vol. 26, p. 100950, mars 2021, doi: 10.1016/j.nme.2021.100950.
[12] Y. Miyoshi *et al.*, *Fusion Eng. Des.*, vol. 156, p. 111568, juill. 2020, doi: 10.1016/j.fusengdes.2020.111568.
[13] M. Kocan *et al.*, *Nucl. Fusion*, vol. 55, n° 3, p. 033019, mars 2015, doi: 10.1088/0029-5515/55/3/033019.
[14] F. Chollet, Deep learning with Python, Manning Publications Co, Shelter Island, New York, 2018.
[15] TensorFlow, Keras », TensorFlow. [En ligne]. Disponible sur: https://www.tensorflow.org/guide/keras?hl=fr.
[16] E. Le Fichoux, « Présentation et utilisation de CAST3M ». 2011. [En ligne]. Disponible sur: http://www-cast3m.cea.fr/html/Documentation_Cast3M/Presentation_Cast3M.pdf.
[17] Q. Tichit *et al.*, *Nucl. Mater. Energy*, vol. 37, p. 101537, déc. 2023, doi: 10.1016/j.nme.2023.101537.
[18] E. Tsitrone, « Overview of plasma wall interactions in the first high particle fluence campaign of WEST », doi: this conference.
[19] A. Gallo *et al.*, *Nucl. Mater. Energy*, vol. 41, p. 101741, déc. 2024, doi: 10.1016/j.nme.2024.101741.